Check for updates

Received: 30 April 2021 | Revised: 21 July 2021 | Accepted: 22 July 2021

DOI: 10.1002/jrs.6221

SPECIAL ISSUE - RESEARCH ARTICLE

Journal of RAMAN SPECTROSCOPY WILEY

Accurate intensity calibration of multichannel spectrometers using Raman intensity ratios

Ankit Raj[1] | Chihiro Kato[2] | Henryk A. Witek[1,3] | Hiro-o Hamaguchi[1,3]

[1]Department of Applied Chemistry and Institute of Molecular Science, National Yang Ming Chiao Tung University, Hsinchu, Taiwan

[2]Department of Chemical Engineering, Kanagawa Institute of Industrial Science and Technology (KISTEC), Ebina, Japan

[3]Center for Emergent Functional Matter Science, National Yang Ming Chiao Tung University, Hsinchu, Taiwan

Correspondence

Ankit Raj, Department of Applied Chemistry and Institute of Molecular Science, National Yang Ming Chiao Tung University, Hsinchu 30010, Taiwan.
Email: ankit@nycu.edu.tw

Hiro-o Hamaguchi, Department of Applied Chemistry and Institute of Molecular Science, National Yang Ming Chiao Tung University, Hsinchu 30010, Taiwan.
Email: hhama@nctu.edu.tw

Funding information

Ministry of Science and Technology, Taiwan, Grant/Award Numbers: MOST103-2113-M- 009-001, MOST105-2923-M-009-001-MY3, MOST108-2113-M-009-010-MY3; Ministry of Education; Center for Emergent Functional Matter Science of National Yang Ming Chiao Tung University

Abstract

We present a general multistep procedure for the determination of wavelength/wavenumber-dependent sensitivity of Raman spectrometers equipped with multichannel detectors. In this approach, we start with photons-per-wavenumber conversion (C_0) followed by a correction (C_1) for the channel-to-channel variation in the sensitivity. The final correction (C_2) is determined from a set of observed intensity ratios for standard Raman bands of selected molecules, compared with the analogous reference set of their accurate theoretical counterparts. The developed approach is employed here for calibrating our Raman spectrometer in the high-wavenumber region using the vibration–rotation Raman bands of H_2, HD, and D_2. Theoretical intensity ratios for these bands were computed using accurate ro–vibrational matrix elements of polarizability invariants. The presented scheme allowed us to significantly improve the accuracy of the relative Raman intensities for measured samples. The accuracy was examined by determining the Boltzmann temperatures from the Raman intensities and comparing them with the corresponding thermocouple measurements. The uncertainty of such a Raman thermometer was found to be within 5%, confirming the validity and robustness of the proposed intensity calibration scheme. The presented intensity correction goes beyond the scope of common calibration schemes, traditionally limited to emission standards like tungsten lamps. While the first two steps of our calibration process (C_0 and C_1) are fairly typical, the additional correction (C_2) derived from Raman spectral intensities seems to constitute an important novel step towards the standardization of Raman spectroscopy.

KEYWORDS

accurate Raman intensities, intensity calibration of Raman spectrometer, relative Raman intensity corrections, standardization of Raman spectroscopy

1 | INTRODUCTION

Multichannel detectors such as photodiode array (PDA), charged coupled device (CCD), and complementary metal-oxide semiconductor (CMOS) detectors are some of the most widely used detectors in various instruments for photon detection. With features like high sensitivity and fast readout over a large array of pixels, they have allowed for significant multiplexing and reduction in measurement durations. The calibration of observed spectra from these detectors, both over the x-axis corresponding to wavelength/wavenumber and over the

 © 2021 John Wiley & Sons, Ltd.

y-axis corresponding to intensities, is an important part of postprocessing of raw spectroscopic data before correct interpretations can be made. Protocols for wavelength/wavenumber calibration using emission-based standards have been well-documented[1,2]; they often utilize electronic emission lines from ionized gases, such as argon/krypon or neon, whose positions have been determined to high accuracy.[3] Using these standards for *x*-axis calibration gives highly accurate results with uncertainties within 0.03–0.1 nm (<4–6 cm^{-1}), in the visible region corresponding to relative uncertainties within 0.5%.

Due to multiple optical components—such as filters for removing/selecting certain wavelengths, mirrors for directing the light beam, and grating for spatial dispersion of light on the detector—involved in the optical path for the detection of Raman scattered photons, a significant distortion in the observed Raman intensities across the measured wavenumber region is observed. This is also evident for single channel detectors, such as photodiodes and photomultipliers, when coupled with dispersive spectrometers. Proper intensity calibration procedure during the data analysis[4,5] becomes important for obtaining accurate spectroscopic intensities and correct interpretations. The determinable information can be related to one or more of the involved factors governing the observed intensities, such as the number of molecules, Boltzmann populations, involved transition moments, and more.[5] Typical corrections for multichannel detectors involve a correction of relative intensities performed using broadband spectra, like white-light emission from heated filament lamps that resembles black body radiation[6,7] and fluorescence emission from known fluorophores, like quinine, Kopp 2412 glass, and coumarin 540a.[8,9] These references, however, suffer from drawbacks, like stability, reproducibility, and spatial dependence of the emission source,[8] and moreover, they require regular recalibrations. It has been noted that intensity calibration using these standards does not suffice for high accuracy applications requiring accuracies higher than 2%.[10–12]

However, if the accurate relative strengths of Raman intensities are known beforehand, either experimentally or theoretically, they can then be used for a straightforward intensity calibration via a direct comparison with observed spectra. In this regard, the present work demonstrates the process of obtaining the sensitivity correction profile over wavelength/wavenumber, by analyzing all the relative Raman intensities. In earlier reports, rotational Raman bands have been used for intensity corrections where the temperature-independent ratios of intensities from common rotational levels have been used to determine the wavenumber dependent sensitivity curve. In particular, Hamaguchi et al. and Montero et al. have used D_2 and H_2, respectively, to determine the wavenumber-dependent correction curve for Raman intensities in a broad wavenumber range.[13,14] Okajima and Hamaguchi have used N_2 for accurate intensity calibration in the low frequency region of the Raman spectrum.[15] In our previous work,[16] we have reported an intensity calibration using pure rotational Raman bands from H_2, HD, and D_2, in combination with the rotation–vibration Raman bands from O_2, which covered the spectral window from −1034 to 1700 cm^{-1}, while taking care of the temperature dependence by considering ratios of observed Raman intensities from common rotational levels.

In the present work, we extend the relative intensity calibration analysis by introducing a generalized treatment of Raman intensities, wherein we focus explicitly on the ratios of intensities of all the observed Raman bands. Some of these ratios are temperature independent, whereas others are temperature dependent. By a comparison with the corresponding theoretical reference ratios, determined via calculations of polarizability invariants, the wavenumber-dependent relative sensitivity and the temperature of the sample are determined using a nonlinear optimization scheme.

This approach is illustrated using the rotation–vibration Raman spectra of H_2, HD, and D_2 consisting of the *O*, *Q*, and *S* branches, recorded in the spectral range from 2500 to 4200 cm^{-1}. This spectral region is important for studies on the CH and OH stretching vibrations and is thus crucial for accurate studies on water. Molecular hydrogen and its isotopes are employed as a reference in the present application; the Raman cross sections and theoretical intensities are computed using the polarizability invariants available from our earlier work.[17] A nonlinear minimization scheme is utilized with a low-degree polynomial representation of the wavenumber-dependent sensitivity. The described numerical techniques are implemented in computer programs written in Python and are available online.[18]

The method introduced here is applicable, in full generality, to Raman bands originating from other gaseous or liquid samples, over an arbitrary spectral range, provided that the measured sample has known polarizability invariants in order to determine the reference intensities. This technique is particularly useful for experiments where information on the anti-Stokes Raman bands is limited or not available. The ultimate outcome of our analysis is the relative intensity correction of our Raman spectrometer in the Stokes region together with the estimate of the Boltzmann temperature of the sample at the focal point, obtained directly from the observed Raman intensities.

2 | METHODOLOGY

In the present approach, the intensity calibration scheme involves three steps.

1. Obtaining correct representation of spectra: we start with a correction C_0 designed for obtaining the correct number of photons-per-wavenumber, necessary for a correct graphical representation and subsequent analysis of the recorded spectra. Photon counting measurements with CCD/CMOS detectors coupled with dispersive spectrographs generally produce spectra from a readout over the horizontal array of pixels (channels), with the x-axis corresponding to a linearly changing wavelength. However, typically the analysis of Raman spectra is performed with the x-axis defined in wavenumbers. Thus, a correction is required to obtain the appropriate number of counted photons per wavenumber, for data originally acquired over a linear wavelength scale. This multiplicative correction is given by $\frac{\delta\nu_s}{\delta\nu_0}$,[19–21] where $\delta\nu_s$ is a vector whose elements are the wavenumber intervals between the consecutive data points of the x-axis defined in wavenumbers and $\delta\nu_0$ is a scalar corresponding to the wavenumber interval at a reference wavenumber ν_0. See Section S1 in the Supporting Information for additional details on this correction.

It is noteworthy to mention that the C_0 correction has only been discussed in context of emission spectroscopy (particularly photoluminescence spectroscopy),[19,20,22] while relevant applications in the field of vibrational spectroscopy have not been reported.

2. Removing channel-to-channel sensitivity differences: the next correction is for the channel-to-channel variation in the sensitivity of the spectrometer. Apart from the effect of nonideal, wavenumber-dependent, transmission/reflectance profiles of the optical components, the dispersive grating and the detectors impart significant wavenumber-dependent variation in the recorded Raman intensities. Moreover, some regions of the spectrum may have large differences in sensitivity due to optical-etaloning/fringing at certain wavelengths or manufacturing imperfections and damages. These non-uniformities in the sensitivity over the detector channels can be effectively accounted for by measurements of a continuous emission, for example, a broadband white-light spectrum from a heated tungsten lamp, which can be assumed to be originating from blackbody emitter. The observed number of photons from such a source per unit solid angle per unit wavenumber[1] is given by

$$I(\nu, T) = 2c\nu^2\left(\frac{1}{e^{\frac{hc\nu}{k_B T}} - 1}\right). \tag{1}$$

The ratio of the observed, C_0-corrected spectra to $I(\nu, T)$ at some assumed temperature T of the emission source gives the next correction (C_1) for the channel-to-channel difference in the sensitivity, which is used subsequently to scale all the observed spectra by dividing them by C_1.

In principle, for heated tungsten lamps, Equation 1 can be evaluated with a known temperature of the lamp if the input current-versus-temperature profile is accurately known. In this case, the multiplicative (C_0/C_1) correction would suffice for intensity calibration.

However, if the temperature of the lamp for a given input current is not known, or if such specifications change over time, then (C_0/C_1) correction would be insufficient for accurate intensity calibration. In most cases, with ordinary lamps, C_0 and C_1 can yield accuracy of around 5–10% in the relative intensities, depending on the size of the analyzed spectral range and the validity of the assumed temperature. For the remaining discrepancies, an additional global correction C_2 derived from the ratios of observed Raman intensities is discussed below. In our understanding, this additional correction constitutes the main accomplishment of the current work.

3. Global correction to sensitivity using spectroscopic data: consider a Raman spectrum having n bands with intensities I_i, $i = 1,\ldots,n$. The ratios of the observed band intensities can be arranged in the form of a $n \times n$ matrix

$$\mathbb{R}_{\text{obs}} = \begin{bmatrix} 1 & \left(\frac{I_2}{I_1}\right)^{-1} & \left(\frac{I_3}{I_1}\right)^{-1} & \cdots & \left(\frac{I_n}{I_1}\right)^{-1} \\ \left(\frac{I_2}{I_1}\right) & 1 & \left(\frac{I_3}{I_2}\right)^{-1} & \cdots & \left(\frac{I_n}{I_2}\right)^{-1} \\ \left(\frac{I_3}{I_1}\right) & \left(\frac{I_3}{I_2}\right) & 1 & \cdots & \left(\frac{I_n}{I_3}\right)^{-1} \\ \vdots & \vdots & \vdots & \ddots & \vdots \\ \left(\frac{I_n}{I_1}\right) & \left(\frac{I_n}{I_2}\right) & \left(\frac{I_n}{I_3}\right) & \cdots & 1 \end{bmatrix}. \tag{2}$$

Similarly, the ratios of true intensities known from either prior experiments or precise calculations can be set up in an analogous matrix $\mathbb{R}_{\text{true}}$. In matrices $\mathbb{R}$, the diagonal terms are equal to unity, whereas the off-diagonal terms have inverse relationship, $\mathbb{R}_{ij} = \mathbb{R}_{ji}{}^{-1}$. Hence, either the lower- or the upper-triangular part contains duplicate

information about the relative intensities. The number of independent terms in the matrices $\mathbb{R}$ are given by $\frac{n(n-1)}{2}$. This is illustrated in Figure 1 using the intensity ratios of four hypothetical bands observed at wavenumber positions from ν_1 to ν_4.

If the Raman spectrum has been acquired on a spectrometer having constant relative sensitivity across the studied wavenumber range, $S(\nu) = 1$, then $\mathbb{R}_{\text{obs}}$ obtained from the experimental intensities and $\mathbb{R}_{\text{true}}$ obtained from theory would be equal. Consequently, one would have

$$\frac{\mathbb{R}_{\text{obs},ij}}{\mathbb{R}_{\text{true},ij}} = 1. \tag{3}$$

However, in practice, the Raman spectrometers have a varying sensitivity across the wavenumber range. This signifies that the ratio $\frac{\mathbb{R}_{\text{obs},ij}}{\mathbb{R}_{\text{true},ij}}$ is different from unity. The numbers

$$\frac{\mathbb{R}_{\text{obs},ij}}{\mathbb{R}_{\text{true},ij}} = \mathbb{S}(\nu_i, \nu_j) \tag{4}$$

can be naturally arranged in a matrix, denoted by $\mathbb{S}$. As done for the band intensities, the matrix $\mathbb{S}$ can be perceived as a matrix of wavenumber-dependent sensitivity ratios

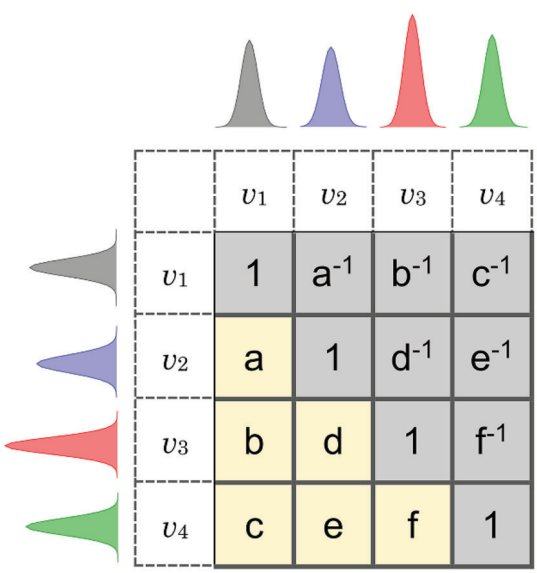

FIGURE 1 Consider four hypothetical Raman bands observed at wavenumbers ν_1–ν_4. Raman intensity ratios among these bands, denoted as a–f ($a = \frac{I_{\nu_1}}{I_{\nu_2}}$, $b = \frac{I_{\nu_1}}{I_{\nu_3}}$, $c = \frac{I_{\nu_1}}{I_{\nu_4}}$, etc.), form a matrix $\mathbb{R}$. the diagonal entries of $\mathbb{R}$ are equal to one, while its lower- and upper-triangular blocks have a reciprocal relationship. In matrix $\mathbb{R}$, the nonredundant information on the relative Raman intensities is contained in the block depicted in yellow [Colour figure can be viewed at wileyonlinelibrary.com]

$$\mathbb{S} = \begin{bmatrix} 1 & \left(\frac{S_{\nu_2}}{S_{\nu_1}}\right)^{-1} & \left(\frac{S_{\nu_3}}{S_{\nu_1}}\right)^{-1} & \cdots & \left(\frac{S_{\nu_n}}{S_{\nu_1}}\right)^{-1} \\ \left(\frac{S_{\nu_2}}{S_{\nu_1}}\right) & 1 & \left(\frac{S_{\nu_3}}{S_{\nu_2}}\right)^{-1} & \cdots & \left(\frac{S_{\nu_n}}{S_{\nu_2}}\right)^{-1} \\ \left(\frac{S_{\nu_3}}{S_{\nu_1}}\right) & \left(\frac{S_{\nu_3}}{S_{\nu_2}}\right) & 1 & \cdots & \left(\frac{S_{\nu_n}}{S_{\nu_3}}\right)^{-1} \\ \vdots & \vdots & \vdots & \ddots & \vdots \\ \left(\frac{S_{\nu_n}}{S_{\nu_1}}\right) & \left(\frac{S_{\nu_n}}{S_{\nu_2}}\right) & \left(\frac{S_{\nu_n}}{S_{\nu_3}}\right) & \cdots & 1 \end{bmatrix}, \tag{5}$$

where each element is expressed as the ratio of wavenumber-dependent sensitivities (S_{ν_i} and S_{ν_j}) at the corresponding wavenumber positions (ν_i and ν_j) for all pairs of bands.

In general, the wavenumber-dependent sensitivity S_ν can be modeled as a smooth function of a continuous variable ν; in the present work, we select for this purpose a polynomial $S_\nu = 1 + \sum c_n \nu^n$. This results in $\mathbb{S}(\nu_i, \nu_j)$ being equal to $\left(\frac{1+\sum c_n \nu_i^n}{1+\sum c_n \nu_j^n}\right)^2$.

In order to determine the coefficients of the polynomial used to model the wavenumber-dependent sensitivity, the difference matrix $\mathbb{D}$ defined as

$$\mathbb{D}_{ij} = \frac{\mathbb{R}_{\text{obs},ij}}{\mathbb{R}_{\text{true},ij}} - \mathbb{S}(\nu_i, \nu_j) \tag{6}$$

is first computed. Specific elements of the matrix $\mathbb{D}$ can be weighted using weights $\mathbb{W}_{ij}$ corresponding to the uncertainties in the experimental data. Moreover, some of the weights can be manually adjusted to promote certain inherent regularities in the Raman intensity ratios, like temperature independence. Our goal is to determine coefficients c_n in such a way that all the elements of the matrix $\mathbb{D}$ become zero. To this end, we define the error as $E = \|\mathbb{D}\|_F^2$, where $\|\mathbb{D}\|_F$ denotes the Frobenius norm of a matrix $\mathbb{D}$, which is subsequently minimized with respect to the coefficients c_n. This procedure, in practice, corresponds to a least-squares fit process, which produces the correction $C_2 \equiv S_\nu = 1 + \sum c_n \nu^n$ corresponding to the wavenumber-dependent sensitivity, used as the final adjustment in our intensity calibration.

Combining the three components in the intensity calibration scheme described above, we arrive at the net multiplicative intensity correction of a Raman spectrometer given as $\left(C_0 / C_1 C_2\right)$. The overall methodology corresponding to this approach is illustrated in Figure S2.

When using vibration–rotation bands from diatomic molecules like H_2 and its isotopologues, the computation

of $\mathbb{R}_{\text{true}}$ requires the knowledge of Raman intensity ratios for specific pairs of bands. Ro–vibrational matrix elements of polarizability invariants, namely, mean polarizability ($\overline{\alpha}$) and polarizability anisotropy (γ), required for obtaining the theoretical Raman intensities were calculated accurately in our earlier work.[17] This dataset includes tabulation of wavelength-dependent matrix elements, with numerical uncertainty of below 1%, for the Raman transitions relevant to this work. The expressions for the parallel polarized Raman intensities of the O, Q, and S vibration–rotation bands from diatomic molecules are given as[5]

$$I_{O(J)} = I_0\,\nu_0\nu_s^3 N F_J\left(\frac{2}{15}\frac{(J+1)(J+2)}{(2J+1)(2J+3)}\langle\gamma\rangle^2_{0,J;1,J-2}\right),$$
$$I_{Q(J)} = I_0\,\nu_0\nu_s^3 N F_J\left(\langle\overline{\alpha}\rangle^2_{0,J;1,J}+\frac{4}{45}\frac{J(J+1)}{(2J-1)(2J+3)}\langle\gamma\rangle^2_{0,J;1,J}\right),$$
$$I_{S(J)} = I_0\,\nu_0\nu_s^3 N F_J\left(\frac{2}{15}\frac{J(J-1)}{(2J-1)(2J+1)}\langle\gamma\rangle^2_{0,J;1,J+2}\right), \tag{7}$$

where I_0 is the incident laser flux, $\nu_0\nu_s^3$ is the frequency factor comprising the laser frequency ν_0 and the scattered light ν_s (in absolute wavenumbers), N is the number of molecules in the focal volume, and F_J accounts for the Boltzmann population factor (including the nuclear spin statistics). The final term in the brackets includes the square of the ro–vibrational matrix elements of wavelength-dependent polarizability invariants, $\langle\overline{\alpha}\rangle_{v,J;v',J'} = \langle\psi_{v,J}|\overline{\alpha}|\psi_{v',J'}\rangle$ and $\langle\gamma\rangle_{v,J;v',J'} = \langle\psi_{v,J}|\gamma|\psi_{v',J'}\rangle$, along with the expanded form of the Placzek–Teller factor, $b_J^{\Delta J=0,\pm2}$. Corresponding expressions for perpendicularly polarized Raman intensities are placed in Section S6.

Intensity ratios among the O, Q, and S bands defined in Equation 7 are categorized into the following six categories (Figure 2):

In these intensity ratios, the incident laser flux (I_0), the laser frequency term (ν_0), and the number of molecules (N) cancel out. Additional simplifications occur for bands originating from the common rotational states for $O(J)$, $Q(J)$, and $S(J)$ Raman transitions because they share the same Boltzmann population factor (exemplified using Figure 3). Hence, intensity ratios from these initial states are temperature independent. In general, these temperature independent terms are of great importance because they allow one to determine Raman spectrometer sensitivity in experiments for which the measurement of temperature in the focal volume is difficult. This is useful for experiments with high power lasers, typically used for gas-phase Raman measurements, or complicated excitation schemes such as multipass setups.

$$a = \frac{I_{O(J_i)}}{I_{O(J_i')}} \qquad d = \frac{I_{Q(J_i)}}{I_{S(J_i')}}$$
$$b = \frac{I_{O(J_i)}}{I_{Q(J_i')}} \qquad e = \frac{I_{Q(J_i)}}{I_{Q(J_i')}}$$
$$c = \frac{I_{O(J_i)}}{I_{S(J_i')}} \qquad f = \frac{I_{S(J_i)}}{I_{S(J_i')}}$$

FIGURE 2 Intensity ratios among the O, Q, and S bands can be classified into six categories. When the initial states for the respective pair of transitions are the same (i.e., $J_i = J_i'$), the specific intensity ratio is temperature independent due to the common Boltzmann population term (see Figures 3 and 7) [Colour figure can be viewed at wileyonlinelibrary.com]

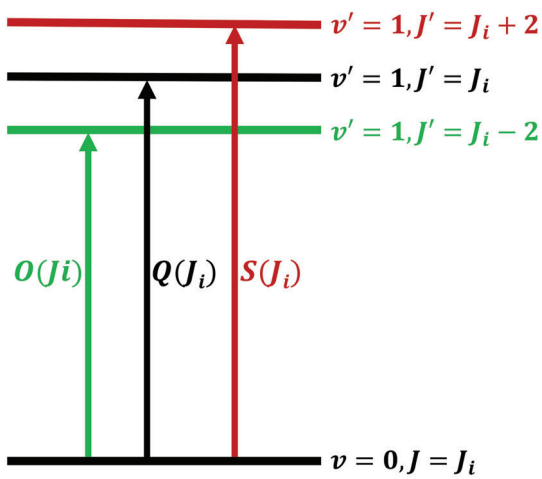

FIGURE 3 O, Q, and S transitions originating from the same initial state share the same Boltzmann population. Hence, the intensity ratios of pairs of such transitions are independent of temperature [Colour figure can be viewed at wileyonlinelibrary.com]

Additional details with a flowchart of the analysis are placed in Section S2. Computer programs implementing this scheme using Python[23,24] are available on GitHub repository.[18]

3 | EXPERIMENTAL

The experimental setup used in the present work has been described earlier.[16] In brief, a laboratory

constructed confocal Raman micro-spectrometer operating with a stabilized 532-nm laser (CW Nd:YVO_4, Verdi-V5, Coherent) was used for excitation. The excitation beam was directed into an inverted microscope (iX71, Olympus) after passing through a Faraday isolator, laser line filter, and a linear polarizer (Glan Taylor prism). A long working distance objective (20×, NA 0.25, $f = 25$ mm, Olympus SLMPLN20×) was used to focus laser beam inside the sample. Backscattered light collected using the same objective lens passed through confocal setup consisting of a 100-μm pinhole. After the confocal setup, Rayleigh scattering was removed using three volume Bragg-notch filters (OptiGrate), followed by Glan–Thomson polarizer (GTH10M-A, Thorlabs) on a rotation mount used as an analyzer. Parallel polarized beam selected using the analyzer was focused on the polychromator slit ($f = 50$ cm, f/6.5, 600 gr/mm grating, SP-2500i, Princeton Instruments, slit width = 120 μm) using an achromatic convex lens, allowing for detection of parallel polarized Raman spectra. Peltier-cooled CCD (DU970N-BV, Andor) operating at −80°C was used as the detector. Diagram with additional details pertinent to the optical setup and measurement system are given in Section S3.

3.1 | Measurement of H_2, HD, and D_2

A custom designed gas cell equipped with heating capabilities mounted on the microscope stage was used for placing gas samples. A mixture of H_2, HD, and D_2 was generated by keeping H_2 and D_2 in approximately 1:1 stoichiometry, at a total pressure of ~3.4 atm and elevated temperature of around 580 K over a period of 12 h. After bringing the mixture to the room temperature, the Raman measurements were performed. Grating position was centered at approximately 645 nm allowing for measurement of the vibration–rotation bands from these gases. Raman measurement was carried out with incident laser power of 200 mW and exposure time of 2.6 h. See Figure 4 for the acquired parallel polarized Raman spectrum, after subtraction of the background signal.

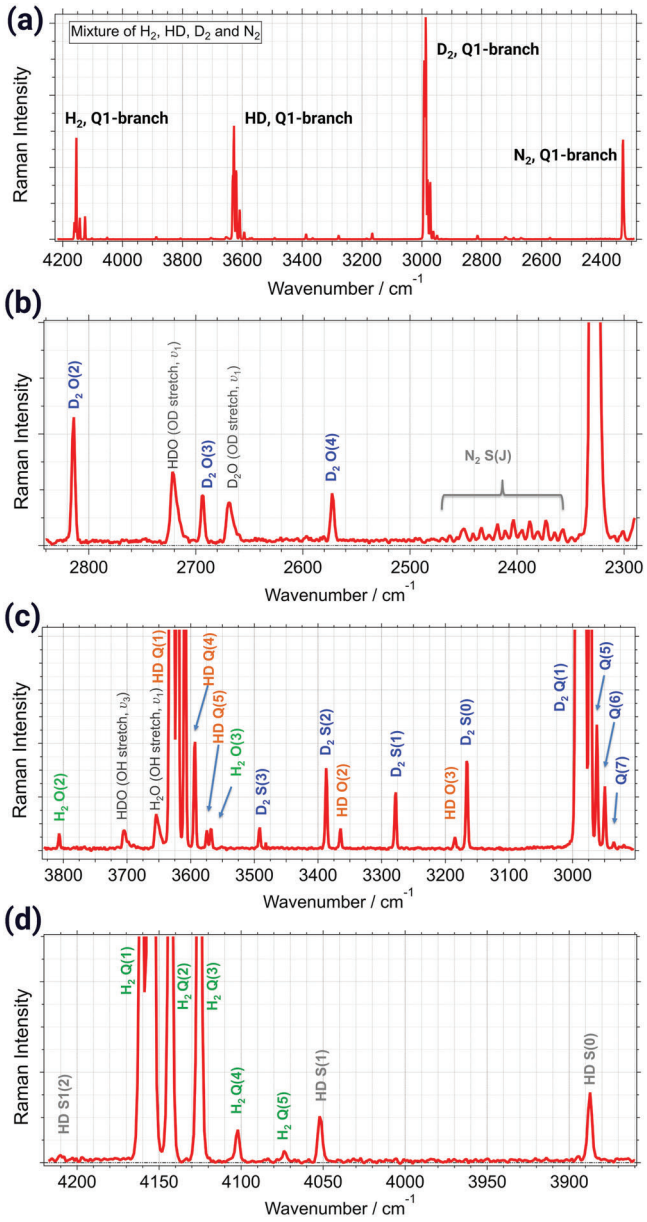

FIGURE 4 Vibration–rotation Raman spectra of a mixture of H_2, HD, and D_2: (a) the full spectral region with the prominent Q branches. (b–d) Zoomed up sections with the assignments. Small amount of N_2, present in the gas cell, is evident by the unresolved Q branch at 2330 cm^{-1}. The contribution of the background has been removed by subtracting the unscaled Raman spectrum of the evacuated cell [Colour figure can be viewed at wileyonlinelibrary.com]

3.2 | Measurement of $CHCl_3$ using 633-nm excitation

Anti-Stokes and Stokes Raman bands of $CHCl_3$ were utilized for temperature determination. Liquid $CHCl_3$ was measured in a quartz cuvette placed on the microscope stage with an average incident laser power of 0.2 mW. Pulsed red laser was introduced in the Raman excitation path using a flipper mirror. This excitation beam at 633 nm was generated using a dye laser based on a 532-nm pulsed laser (10 ns, 500 Hz) and used DCM dye (Exciton) dissolved in ethanol as the fluorophore. The dye recirculated through a cell placed in a laser cavity aligned in a Littrow configuration. The collection path of the Raman spectrometer was undisturbed except for the introduction of a notch filter for the rejection of Rayleigh scattering at 633 nm. The sole purpose of this

measurement is a validation of the intensity calibration procedure described in this study.

4 | DATA ANALYSIS

Figure 4a shows the recorded vibration–rotation Raman spectrum of the gas mixture in the high-wavenumber region, after the subtraction of background signal (acquired from the evacuated gas cell). The strongest bands are the Q branches ($\Delta v = 1, \Delta J = 0$) of molecular hydrogen and its isotopologues. The much weaker bands spreading between the strong Q branches are the O ($\Delta v = 1, \Delta J = -2$) and the S bands ($\Delta v = 1, \Delta J = +2$) from H_2, HD, and D_2. The unresolved Q branch from N_2 was also observed at 2330 cm^{-1}, due to the presence of small amount of air as an impurity in the gas cell. A detailed assignment of all the observed bands was performed before the application of the band positions and their intensities for calibration purposes.

Magnified portions of the spectra discussed above are shown in Figure 4b–d with the assignments of the observed peaks. In Figure 4b, three of the O bands from D_2 are observed along with the unresolved Q branch and the resolved S bands of N_2. In Figure 4c, the partially resolved Q branches of D_2 and HD are the major spectral features along with the S bands from D_2 and O bands from HD and H_2. Lastly, the high-frequency end of the spectrum shown in Figure 4d consists of the resolved Q branch of H_2 and the S bands of HD.

In the case of N_2, the band center of the Q band was used for wavenumber calibration. Because only the S bands of N_2 were recorded due to the limited spectral window, band intensities from N_2 were not used for the purpose of relative intensity calibration because the corresponding O bands were not available in our experiments. Raman features of the O–D and O–H stretches from traces of H_2O and its isotopologues were also observed, which however, were not utilized in the present work.

After an identification of all the features in the recorded spectra, wavenumber calibration in this high-wavenumber region was carried out using the vibration–rotation bands of H_2 and its isotopologues and the band center of the unresolved Q branch of N_2. Raman transition wavenumbers obtained from accurate theoretical datasets on the dissociation energies of ro–vibrational states of H_2 and its isotopologues[25,26] and reported experimental results on N_2, were used for this purpose. A least-squares fit of the band positions (in pixels) against the reference Raman transition wavenumbers (in cm^{-1}) was performed to obtain the polynomial coefficients, governing the pixel-to-wavenumber relationship. The obtained residuals in both the x- and y-values were converted to the corresponding 3σ values; the largest of these 3σ values was 0.4 cm^{-1}. The fit is shown in Section S4.

For intensity calibration, the C_0 correction was computed first. This is shown in Figure 5.

Next, the C_1 correction was obtained from acquired wavenumber-dependent intensities ($W_{obs}(\nu)$) in the broadband white-light spectrum as follows: (i) the acquired white-light spectrum was first corrected with the C_0 correction obtained earlier. (ii) The C_0-corrected white-light spectrum was fitted using Equation 1 for the number of photons per wavenumber, $f(\nu, T_{fit})$, with the temperature of the lamp (T_{fit}) obtained as a fit parameter. (iii) Lastly, the C_1 correction was determined as the ratio of the corrected white-light spectra and its fit, $f(\nu, T_{fit})$, as $C_1 = \frac{W_{obs}(\nu)}{f(\nu, T_{fit})}$.

The determination of the C_1 correction is shown in Figure 6, where the C_0-corrected white-light spectra and its fit $f(\nu, T_{fit})$ are displayed in blue and red, respectively. The C_1 correction is shown in gray.

Noticeably, the broadband white-light spectrum shows a gradual reduction in the intensity beyond 3600 cm^{-1} and a significant drop after 4000 cm^{-1}. Overall, this is due to the loss of performance of the grating and the decreasing detection efficiency of the detector at these higher wavelengths (>655 nm). Figure 6 demonstrates the importance of using the second correction (defined as C_1) for the channel-to-channel variation in the sensitivity.

In order to obtain the final correction (C_2), the band areas of various vibration–rotation Raman bands of H_2, HD, and D_2 were determined using band fitting, after the

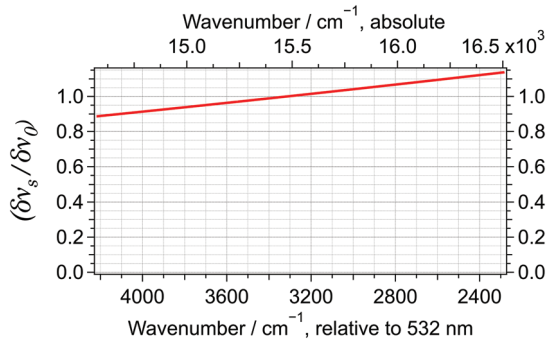

FIGURE 5 A correction $C_0 = \delta\nu_s/\delta\nu_0$ is required to obtain a spectrum represented as photons per wavenumber from a spectrum originally measured as photons per wavelength. The C_0 correction was scaled to unity at the center of the studied here spectral region. The characteristic of this correction strongly depends on the specific spectrograph and the grating position used in the experiment [Colour figure can be viewed at wileyonlinelibrary.com]

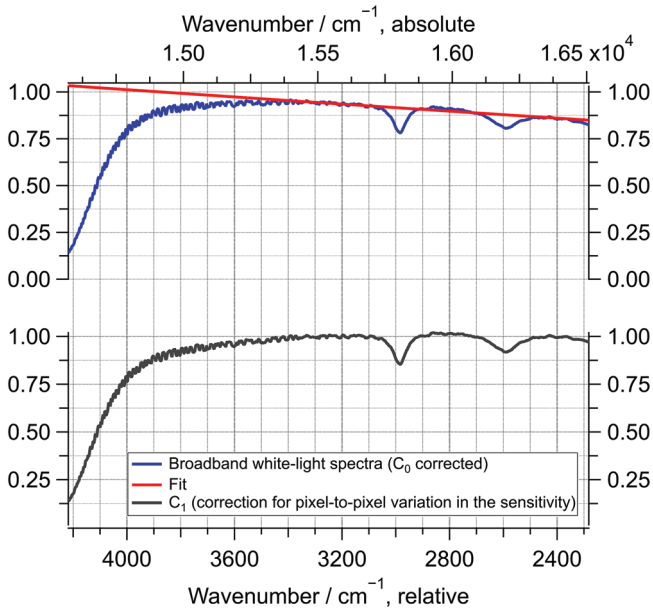

FIGURE 6 A correction C_1 for the pixel-to-pixel difference in the wavenumber-dependent sensitivity in the studied spectral region. This correction (black line) was obtained by a ratio of the observed broadband white-light spectra (blue line) to the fit, assuming black-body emission (red line). Note that the sensitivity of our Raman spectrometer drops considerably over 4000 cm^{-1} [Colour figure can be viewed at wileyonlinelibrary.com]

acquired spectrum was corrected using a multiplicative factor of (C_0/C_1) found earlier. In the acquired Raman spectra, the O and S bands are fully resolved, but the Q branches were only partially resolved. In order to determine the individual band areas of the $Q(J)$ bands, a constrained band fitting was performed. In this process, the peak positions of the bands were fixed to theoretically determined, accurate Raman transition frequencies obtained from reported datasets.[25,26] Plots showing the band fitting with the residuals are placed in Section S6.

Three $\mathbb{R}_{\text{obs}}$ matrices were constructed, one for each of the gases, using selected vibration–rotation bands having relatively high signal-to-noise ratios (this corresponded to six Raman bands from H_2, eight from HD, and 13 from D_2; see Figure 7 for more details). The analogous three $\mathbb{R}_{\text{true}}$ matrices were computed using the expressions for the intensity ratios (among the O, Q, and S bands) described earlier in Figure 2 and the ro–vibrational matrix elements of polarizability invariants available from our earlier work.[17] See Section S4 for a full tabulation of the polarizability invariants and their uncertainties, relevant to the studied Raman transitions. Details on the computation of the Boltzmann populations of the initial states for the Raman transitions studied in this work are given in Section S2.

The detailed structure of the $\mathbb{R}$ matrices for the three studied gases is illustrated in Figure 7; various intensity ratios are represented using the color code defined earlier in Figure 2. The net error is defined as $E = \|\mathbb{D}_{H_2}\|_F^2 + \|\mathbb{D}_{HD}\|_F^2 + \|\mathbb{D}_{D_2}\|_F^2$, where $\|\mathbb{D}\|_F$ denotes the Frobenius norm of a matrix $\mathbb{D}$ defined as $\|\mathbb{D}\|_F = \sqrt{\sum_i \sum_j |d_{ij}|^2}$. Our goal here is to find the coefficients c_n in the polynomial $1 + \sum c_n \nu^n$ and the temperature T_{analysis}. These quantities were obtained by a minimization of E using a nonlinear least-squares fitting procedure implemented in Python[23] and based on the **OPTIMIZE** library in SciPy.[24,27–29] We used a numerical optimization scheme, starting from some presumed guess values (more details are given in Section S2). Several combinations of initial parameters were tested in order to guarantee that the obtained solution corresponds to a physically meaningful, global minimum. The solution is obtained iteratively, by updating the guess values until the associated gradient vanishes. The degree of the employed polynomial $1 + \sum c_n \nu^n$ was set to 2; however, other values (from 1 to 5) were also tested. The number of iterations needed to obtain convergence was usually in the range of 50–100.

The obtained final correction (C_2), modeled as a quadratic polynomial, is shown in Figure 8a; the corresponding residual plots obtained using linear, quadratic, and cubic polynomials are shown in Figure 8b. Additional details covering the nonlinear optimization process and the C_2 curves corresponding to the tested polynomials are shown in Section S2.

4.1 | Error analysis

The sources and estimated magnitudes of errors in our analysis are discussed below.

The elements $\mathbb{R}_{\text{obs},ij}$ have uncertainties arising due to the error in the respective experimental Raman band intensities. The uncertainty in the Raman band area includes two components: (i) the statistical error in the Raman band areas estimated by repeating the measurements at various exposure times, giving an overview of the magnitude of error against the recorded total photon counts, and (ii) the error originating from the peak fitting procedure (see Section S7 for more details). The overall uncertainty for the ith band was estimated as $\sigma_{i,\text{exp}} = \sqrt{\sigma_{i,\text{statistical}}^2 + \sigma_{i,\text{peak fitting}}^2}$. The uncertainty in the ratio $\mathbb{R}_{\text{obs},\ ij}$ was then obtained as $\sigma_{ij,\text{total}} = \frac{I_i}{I_j}\sqrt{\left(\frac{\sigma_{i,\text{exp}}}{I_i}\right)^2 + \left(\frac{\sigma_{j,\text{exp}}}{I_j}\right)^2}$. The corresponding element of the weight matrix ($\mathbb{W}$) was then computed as $w_{ij} = 1/\sigma_{ij,\text{total}}^2$. These weights, derived from experimental

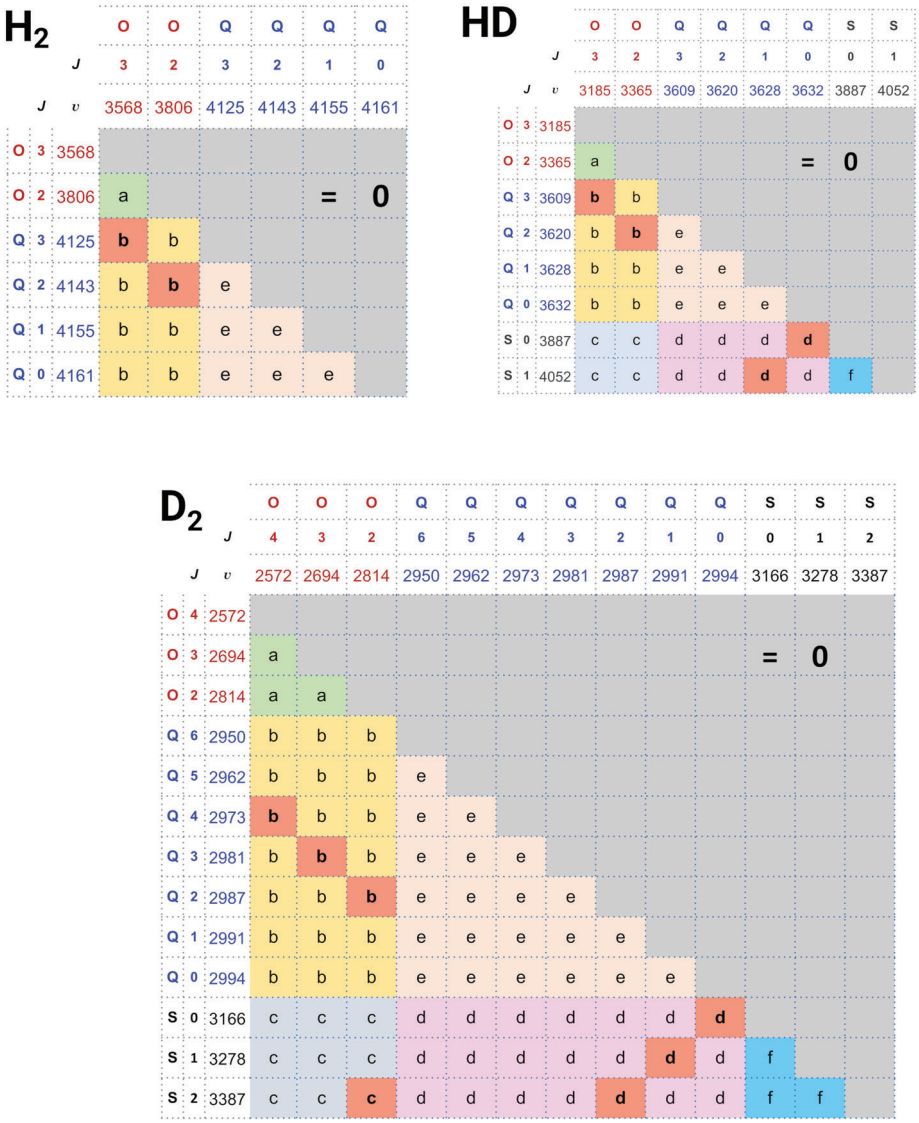

FIGURE 7 Structure of the matrices $\mathbb{R}_{\text{obs}}$ and $\mathbb{R}_{\text{true}}$ for the present experimental dataset. The lower triangular block of the matrix represents the intensity ratios of the specific pairs of studied Raman transitions. The diagonal along with the upper-triangular block contains redundant information and was manually set to zero. Terms a–f represent the intensity ratios defined earlier, following the color scheme defined in Figure 2. Most importantly, the elements in red shaded boxes are the temperature independent terms and correspond to pair of transitions originating from the same initial state ($J_i = J_i'$). These elements were given higher weights ($\times 10$) in our analysis [Colour figure can be viewed at wileyonlinelibrary.com]

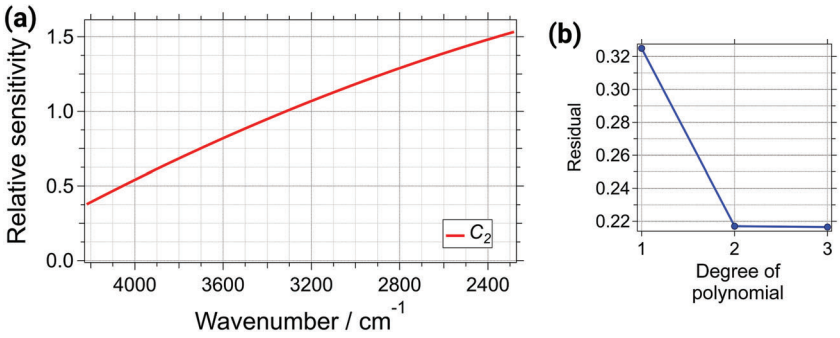

FIGURE 8 (a) A final correction (C_2) obtained using the analysis of relative experimental and theoretical Raman intensities of H_2 and its isotopologues. (b) Residuals (i.e., minimized values of E) obtained using linear, quadratic, and cubic polynomials in the fit for determining the C_2 correction. It is clear that the second-order polynomial is sufficient to represent the wavenumber dependence of C_2 [Colour figure can be viewed at wileyonlinelibrary.com]

uncertainties, were then used to scale the specific elements of the difference matrix ($\mathbb{D}$) in the fitting analysis (described earlier in Section 2). With regard to the present experiments, errors in the experimental intensities were dominated by statistical errors for the O and S bands and peak fitting error for the Q bands. The net uncertainties in the intensity ratios ($\sigma_{ij,\text{total}}$) were 2–12%.

The elements of the matrix $\mathbb{R}_{true}$ have uncertainties originating from the computation of the respective Raman intensities. This includes (i) error in the values of the square of matrix elements of polarizability invariants, which was estimated to be below 0.4%, and (ii) the error in the computed Boltzmann populations of the involved initial states, which was estimated to be below 0.5%. The net error in the elements of the $\mathbb{R}_{true}$ matrix was found to be below 1% (see Section S8 for more details).

Overall, the principal contribution to the net error in the present analysis originates from the experimental data, which affects the elements of the matrix $\mathbb{R}_{obs}$. This uncertainty was included in our fitting by first, constructing the weight matrix using the respective uncertainties, followed by scaling the elements of the difference matrix with the corresponding element of the weight matrix. The error in the elements of the $\mathbb{R}_{true}$ matrix was significantly small compared with the error in the corresponding elements of $\mathbb{R}_{obs}$. Hence, the uncertainty in $\mathbb{R}_{true}$ was neglected in the present fitting analysis. The reader should bear in mind that another component of the weights w_{ij} does not correspond to the experimental uncertainties but is at our hand to promote specific temperature independent elements of the matrix $\mathbb{D}$, as discussed earlier in Section 4.

5 | RESULTS

Measured vibration–rotation Raman spectra of H_2, HD, and D_2 are shown in Figure 4. The C_0 and C_1 corrections are plotted in Figures 5 and 6, respectively. The C_2 correction obtained from the present analysis, assuming a quadratic polynomial, is shown in Figure 8a. The corresponding plot of the residuals obtained using linear, quadratic, and cubic polynomial representations of C_2 is shown in Figure 8b. Convergence of the optimization was monitored by checking the residual that changed minutely when going from quadratic to cubic polynomial (see Section S2 for C_2 curves obtained from the tested polynomials).

The present analysis for the final correction to the Raman intensities (i.e., C_2) obtained from the acquired Raman spectra includes temperature $T_{analysis}$ as an independent fit variable. Hence, the temperature value obtained from our numerical analysis could be compared with the value recorded during the Raman measurement ($T_{expt.}$), in order to verify the fit results; the difference was found to be 1.3 K (see Table 1 for the respective temperatures and the difference). This result shows an advantage of the present scheme to obtain the relative sensitivity of the spectrometer and the temperature of the sample in the focal volume, in a straightforward analysis.

The accuracy of the intensity calibration in the high-wavenumber region was independently checked by the following approaches:

1. Temperature determination from vibration–rotation bands of H_2 and isotopologues: relative Raman intensities among the vibration–rotation bands were used with the known matrix elements of polarizability invariants, in a least-squares fitting scheme to determine the temperature from the Boltzmann factors. Such an approach has been recently described by Capek and coworkers.[30] The results obtained from band area derived from both the uncorrected and intensity calibrated Raman spectra are shown in Table 2. Uncorrected spectra show widely varying temperatures across the analyzed spectral range, with large difference from the temperature recorded during experiments (~299 K). After intensity correction using the C_2 term, a significant improvement in the

TABLE 1 The Boltzmann temperature (in K) obtained from the analysis of the C_2 correction, with the experimental temperature recorded using a thermocouple

$T_{analysis}$	$T_{expt.}$[a]	Difference
298.2	299.5	1.3

[a]With uncertainty of ±0.7 K.

TABLE 2 Comparison of the Boltzmann temperatures (in K) determined from Raman intensities before and after the C_2 correction

Transitions	Spectral region	Temperature	
	cm^{-1}	After C_0, C_1 corrections	After C_0, C_1, C_2 corrections
D_2, $Q(0)$, (1) and (2)	2987–2993	292.2	300.8
HD, $Q(0)$ (1) and (2)	3609–3632	296.2	301.9
H_2, $Q(0)$ (1) and (2)	4143–4161	326.1	306.2
D_2, $O(2)$ and $S(0)$ bands	3814 and 3166	390.5	308.6

Note: The corresponding temperature recorded using a thermocouple was 299.5 (±0.7) K.

determined temperature value was observed. For narrow spectral regions, this discrepancy was as small as 1 K, whereas for broader regions, it is up to 9 K.

2. Temperature determination from anti-Stokes and Stokes Raman bands of $CHCl_3$: Raman spectra of liquid chloroform was measured using a 633-nm pulsed laser introduced to the microscope stage using a movable mirror without modification to the collection path of the Raman spectrometer, except for the introduction of a notch filter for 633-nm Rayleigh rejection. The grating position was unchanged during this measurement. Transmission profile of this filter across the present spectral range is shown in Figure 9, along with the recorded Raman spectra of chloroform. Transmission curve of the notch filter was included in the analysis when determining the band area after intensity calibration of the acquired spectra. Temperature of the sample was determined using the anti-Stokes and Stokes band area ratios using the relationship: $\frac{I_{\text{anti-Stokes}}}{I_{\text{Stokes}}} \times \frac{(\nu_0-\nu)^3}{(\nu_0+\nu)^3} = e^{-\frac{hc\nu}{kT}}$. The Boltzmann temperatures determined utilizing the 366 and 667 cm^{-1} bands of chloroform (and their anti-Stokes counterparts, all defined relative to 633 nm) were 294 and 301 K, respectively. The actual temperature of the liquid recorded using a thermocouple was 299.5 (±0.7) K. The deviations in temperature obtained using our Raman thermometer indicate errors of around 3% in the relative intensities in the spectral range 2310–3652 cm^{-1} (relative to 532 nm).

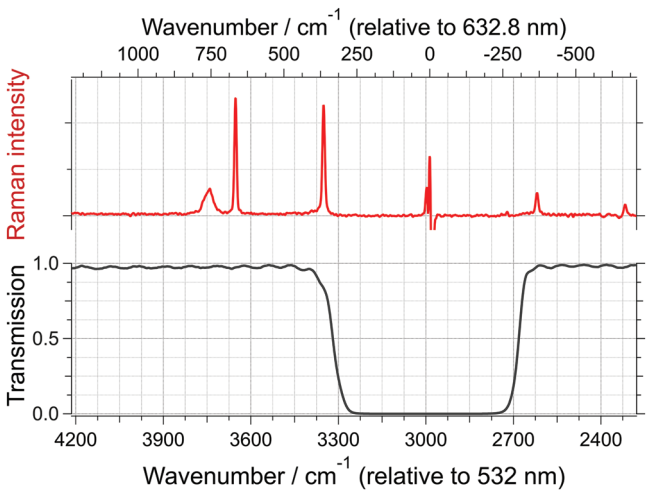

FIGURE 9 Raman spectrum of $CHCl_3$ featuring two pairs of anti-stokes and stokes bands, measured using 633-nm pulsed laser for testing the accuracy of the proposed intensity calibration procedure. This spectral region corresponds to the high-wavenumber region studied in the present work using 532-nm laser. Transmission curve (T_{notch}) of the notch-filter, introduced in the collection path of the Raman spectrometer, is shown in black. The intensity-corrected Raman spectrum of $CHCl_3$ was scaled by ($1/T_{\text{notch}}$) before the determination of the respective band areas [Colour figure can be viewed at wileyonlinelibrary.com]

6 | DISCUSSION

The relative intensity calibration procedure presented in this work relies on using the observed Raman intensities to extract the wavenumber-dependent sensitivity after the C_0 and C_1 corrections. The C_2 correction is necessary because C_1, used in the previous step, is only an approximation. During the evaluation of the C_1 correction, it is assumed that the emission characteristics of the lamp obey the black-body emission profile. Further, any spatial non-uniformity of the broadband light on the observed focal plane and its spectral modulation before entering the Raman photon collection path is disregarded.

The C_2 correction can be determined, in principle, using any set of Raman bands that can be precisely measured and for which the corresponding reference intensities can be accurately computed or are available from prior studies. We used Raman bands from molecular hydrogen and its isotopologues to determine the C_2 correction, following the methodology initiated in our previous study.[16] This approach has a number of distinct advantages: numerous well-defined Raman bands of H_2, HD, and D_2 cover a broad spectral range, simple molecular structure of hydrogen allows one to calculate the polarizabilities and ro–vibrational wave functions with high accuracy, and detailed knowledge on the accurate Raman transition frequencies facilitates a simultaneous wavenumber calibration.

In our previous work, we used the pure rotational Raman spectra of H_2, HD, and D_2 to determine the C_2 correction for the spectral range from −1100 to 1640 cm^{-1}, covering the anti-Stokes and Stokes regions. In this study, we extend the calibration to the high-wavenumber spectral region (from 2300 to 4200 cm^{-1}), now using the vibration–rotation Raman bands of H_2, HD, and D_2, in addition presenting a more general treatment of the relative Raman intensities. The following drawbacks can be identified in conjunction with employing vibration–rotation bands in our analysis, instead of the pure-rotational Raman bands used in our previous work.

- Small Raman cross sections of the vibration–rotation bands of H_2, HD, and D_2 demanded longer accumulation times for acquiring quality Raman spectra. For example, the present experiment required about five

times longer duration of spectral acquisitions to achieve signal-to-noise ratios comparable with our previous work based on the pure rotational Raman bands. The stability of the Raman spectrometer for such long experiments and any change to the performance of the optical components due to high laser powers will also affect the results.

- The strong polarization dependence of the Q vibration–rotation Raman bands might be an obstacle when using the developed here procedure for accurate calibration of Raman spectrometers not permitting sufficient resolution of polarized Raman photons. The $Q(J)$ bands are the most prominent features in the vibration–rotation spectrum; they are highly polarized and feature J-dependent depolarization ratios. This requires specialized optical elements in the Raman spectrometer for generating a linearly polarized excitation beam and for resolving with sufficient accuracy the two polarizations in the Raman collection path. Failing to do so contributes additional uncertainty to the recorded experimental Raman intensities, and degrading the accuracy of the obtained C_2 correction, which relies to a large extent on the Q band intensities. Further tests were performed to check this phenomenon. An extension of the proposed here calibration procedure to the Raman dataset for perpendicularly polarized detection is presented in Section S6, where we utilize the perpendicularly polarized vibration–rotation Raman bands of H_2, HD, and D_2 to determine an analogous C_2 correction. The corresponding error analysis shows that the accuracy of such a calibration is somewhat lower than of that presented here for parallel polarization. The depolarization ratios showed small deviations from the true values indicating the limit of the polarization separation ability of the present instrument.

7 | CONCLUSION

A multistep intensity calibration procedure is presented in detail, where inconsistencies in the relative Raman intensities are corrected using a three-component correction comprising (i) C_0 corresponding to photons-per-wavenumber conversion, (ii) C_1 for pixel-to-pixel sensitivity correction, and lastly (iii) C_2 obtained from an analysis of the ratios of experimental Raman intensities.

The hydrogen isotopologues, owing to their large rotational constants, yield Raman bands that span a broad spectral range. Simple structure of molecular hydrogen allows for accurate determination of its ro–vibrational wave functions and polarizability invariants, required for explaining Raman transition frequencies and intensities. These features make the observed Raman bands from these molecules particularly suitable for calibration purposes in Raman spectroscopy.

In the present analysis, the vibration–rotation bands from H_2, HD, and D_2 were used for calibrating our Raman spectrometer in the spectral region from 2300 to 4200 cm^{-1}. After the standard C_0 and C_1 corrections to the spectral intensities, the relative Raman intensities from the recorded Raman bands of these gases were used to determine the C_2 correction modeled as a polynomial. Boltzmann temperature of the sample in the focal volume was determined simultaneously as a fit parameter along with the coefficients of the polynomial. Error in the calibrated relative Raman intensities was found to be around 3%. Further accuracy improvements are possible by increasing the signal-to-noise ratio of the recorded Raman intensities used for obtaining C_2, for example, by measurements at an elevated temperature. The presented scheme for relative intensity calibration is easily extensible to even higher wavenumber region by including the S bands from H_2 attainable via measurements at different grating positions or using a lower resolution spectrograph. The accurate calibration of the studied high-wavenumber region is crucial for studying the Raman intensities of CH and OH stretch vibrations, as well as combinations and overtones.

ACKNOWLEDGEMENTS

This work was supported by Ministry of Science and Technology, Taiwan (Grant Nos. MOST105-2923-M-009-001-MY3, MOST108-2113-M-009-010-MY3, and MOST103-2113-M-009-001) and the Center for Emergent Functional Matter Science of National Yang Ming Chiao Tung University from the Featured Areas Research Center Program within the framework of the Higher Education Sprout Project by the Ministry of Education (MOE), Taiwan. AR is thankful to Dr. Rintaro Shimada (University of Tokyo) for suggestions on experiments for validation using 633-nm excitation. Dr. Sudhakar Narra (NYCU) is acknowledged for help with alignment of the dye laser.

DATA AVAILABILITY STATEMENT

Programs written in Python are available on GitHub and indexed with the https://doi.org/10.5281/zenodo.4655294.

ORCID

Ankit Raj https://orcid.org/0000-0002-2495-3354
Henryk A. Witek https://orcid.org/0000-0002-9013-1287
Hiro-o Hamaguchi https://orcid.org/0000-0002-4320-0921

ENDNOTES

[1] ν in Equation 1 is defined in absolute wavenumbers.

[2] In practical implementation, to enhance the numerical accuracy of the fitting procedure, the wavenumber range is rescaled to [−1,1], and care is taken that the sensitivity at the rescaled ν_0 is unity.

REFERENCES

[1] H. Hamaguchi, *Appl. Spectrosc. Rev.* **1988**, *24*(1–2), 137.
[2] J. Loader, *Basic Laser Raman spectroscopy*, Heyden and Sons Ltd., London **1970**.
[3] A. Kramida, Y. Ralchenko, J. Reader, and NIST ASD Team, in NIST Atomic Spectra Database (version 5.7.1) (National Institute of Standards and Technology, Gaithersburg, MD, **2019**).
[4] R. L. McCreery, *Raman Spectroscopy for Chemical Analysis*, J. Wiley, New York **2000**.
[5] D. A. Long, *The Raman Effect : A Unified Treatment of the Theory of Raman Scattering by Molecules*, Wiley, New York **2003**.
[6] I. Langmuir, *Phys. Rev.* **1916**, *7*(3), 302.
[7] R. Stair, W. E. Schneider, J. K. Jackson, *Appl. Opt.* **1963**, *2*(11), 1151.
[8] K. Iwata, H. Hamaguchi, M. Tasumi, *Appl. Spectrosc.* **1988**, *42*(1), 12.
[9] K. G. Ray, R. L. McCreery, *Appl. Spectrosc.* **1997**, *51*(1), 108.
[10] K. T. Schomacker, J. K. Delaney, P. M. Champion, J. Chem, *Phys.* **1986**, *85*(8), 4240.
[11] C. M. Penney, R. L. S. Peters, M. Lapp, J. Opt, *Soc. Am.* **1974**, *64*(5), 712.
[12] C. M. Penney, M. Lapp, J. Opt, *Soc. Am.* **1976**, *66*(5), 422.
[13] H. Hamaguchi, I. Harada, T. Shimanouchi, *Chem. Lett.* **1974**, *3*(12), 1405.
[14] S. Montero, D. Bermejo, M. A. Lopez, *Appl. Spectrosc.* **1976**, *30*(6), 628.
[15] H. Okajima, H. Hamaguchi, *J Raman Spectrosc* **2015**, *46*(11), 1140.
[16] A. Raj, C. Kato, H. A. Witek, H. Hamaguchi, *J Raman Spectrosc* **2020**, *51*(10), 2066.
[17] A. Raj, H. Hamaguchi, H. A. Witek, *J. Chem. Phys.* **2018**, *148*(10), 104308.
[18] A. Raj, IntensityCalbr: an open-source repository for programs in Python implementing scheme for intensity calibration using relative Raman intensities, **2020**. (https://github.com/ankit7540/IntensityCalbr)
[19] G. Angulo, G. Grampp, A. Rosspeintner, *Spectrochim. Acta a Mol. Biomol. Spectrosc.* **2006**, *65*(3), 727.
[20] J. Mooney, P. Kambhampati, *J. Phys. Chem. Lett.* **2013**, *4*(19), 3316.
[21] J. Mooney, P. Kambhampati, *J. Phys. Chem. Lett.* **2014**, *5*(20), 3497.
[22] B. Valeur, *Molecular Fluorescence: Principles and Applications*, Wiley-VCH, New York **2001**.
[23] T. E. Oliphant, *Computing in Science & Engineering* **2007**, *9*(3), 10.
[24] P. Virtanen, R. Gommers, T. E. Oliphant, M. Haberland, T. Reddy, D. Cournapeau, E. Burovski, P. Peterson, W. Weckesser, J. Bright, S. J. van der Walt, M. Brett, J. Wilson, K. J. Millman, N. Mayorov, A. R. J. Nelson, E. Jones, R. Kern, E. Larson, C. J. Carey, İ. Polat, Y. Feng, E. W. Moore, J. VanderPlas, D. Laxalde, J. Perktold, R. Cimrman, I. Henriksen, E. A. Quintero, C. R. Harris, A. M. Archibald, A. H. Ribeiro, F. Pedregosa, P. van Mulbregt, A. Vijaykumar, A. P. Bardelli, A. Rothberg, A. Hilboll, A. Kloeckner, A. Scopatz, A. Lee, A. Rokem, C. N. Woods, C. Fulton, C. Masson, C. Häggström, C. Fitzgerald, D. A. Nicholson, D. R. Hagen, D. V. Pasechnik, E. Olivetti, E. Martin, E. Wieser, F. Silva, F. Lenders, F. Wilhelm, G. Young, G. A. Price, G.-L. Ingold, G. E. Allen, G. R. Lee, H. Audren, I. Probst, J. P. Dietrich, J. Silterra, J. T. Webber, J. Slavič, J. Nothman, J. Buchner, J. Kulick, J. L. Schönberger, J. V. de Miranda Cardoso, J. Reimer, J. Harrington, J. L. C. Rodríguez, J. Nunez-Iglesias, J. Kuczynski, K. Tritz, M. Thoma, M. Newville, M. Kümmerer, M. Bolingbroke, M. Tartre, M. Pak, N. J. Smith, N. Nowaczyk, N. Shebanov, O. Pavlyk, P. A. Brodtkorb, P. Lee, R. T. McGibbon, R. Feldbauer, S. Lewis, S. Tygier, S. Sievert, S. Vigna, S. Peterson, S. More, T. Pudlik, T. Oshima, T. J. Pingel, T. P. Robitaille, T. Spura, T. R. Jones, T. Cera, T. Leslie, T. Zito, T. Krauss, U. Upadhyay, Y. O. Halchenko, Y. Vázquez-Baeza, C. SciPy, *Nat. Methods* **2020**, *17*(3), 261.
[25] J. Komasa, K. Piszczatowski, G. Łach, M. Przybytek, B. Jeziorski, K. Pachucki, J. Chem, *Theory Comput.* **2011**, *7*(10), 3105.
[26] K. Pachucki, J. Komasa, *Phys. Chem. Chem. Phys.* **2010**, *12*(32), 9188.
[27] J. Nocedal, S. J. Wright, *Numerical Optimization*, Springer, New York, NY **2006**.
[28] J. E. Dennis, R. B. Schnabel, *Numerical Methods for Unconstrained Optimization and Nonlinear Equations*, Society for Industrial and Applied Mathematics, Philadelphia **1996**.
[29] W. H. Press, S. A. Teukolsky, W. T. Vetterling, B. P. Flannery, *Numerical Recipes 3rd Edition: The Art of Scientific Computing*, Cambridge University Press, Cambridge, UK **2007**.
[30] T. Capek, J. Borysow, C. Mazzoleni, M. Moraldi, *Remote Sensing* **2020**, *12*(24), 4129.

SUPPORTING INFORMATION

Additional supporting information may be found online in the Supporting Information section at the end of this article.

How to cite this article: A. Raj, C. Kato, H. A. Witek, H. Hamaguchi, *J Raman Spectrosc* **2021**, 1. https://doi.org/10.1002/jrs.6221